RSC Advances

PAPER

View Article Online
View Journal | View Issue

Cite this: *RSC Adv.*, 2020, **10**, 30746

Thermally-stable high energy storage performances and large electrocaloric effect over a broad temperature span in lead-free BCZT ceramic

Zouhair Hanani, *[ab] Soukaina Merselmiz, [a] Daoud Mezzane, [a] M'barek Amjoud, [a] Andraž Bradeško, [c] Brigita Rožič, [c] Mohammed Lahcini, [ad] Mimoun El Marssi, [e] Andrey V. Ragulya, [f] Igor A. Luk'yanchuk, [eg] Zdravko Kutnjak [c] and Mohamed Gouné [b]

$Ba_{0.85}Ca_{0.15}Zr_{0.10}Ti_{0.90}O_3$ (BCZT) relaxor ferroelectric ceramics exhibit enhanced energy storage and electrocaloric performances due to their excellent dielectric and ferroelectric properties. In this study, the temperature-dependence of the structural and dielectric properties, as well as the field and temperature-dependence of the energy storage and the electrocaloric properties in BCZT ceramics elaborated at low-temperature hydrothermal processing are investigated. X-ray diffraction and Raman spectroscopy results confirmed the ferroelectric–paraelectric phase transition in the BCZT ceramic. At room temperature and 1 kHz, the dielectric constant and dielectric loss reached 5000 and 0.029, respectively. The BCZT ceramic showed a large recovered energy density (W_{rec}) of 414.1 mJ cm^{-3} at 380 K, with an energy efficiency of 78.6%, and high thermal-stability of W_{rec} of 3.9% in the temperature range of 340–400 K. The electrocaloric effect in BCZT was explored *via* an indirect approach following the Maxwell relation at 60 kV cm^{-1}. The significant electrocaloric temperature change of 1.479 K at 367 K, a broad temperature span of 87 K, an enhanced refrigerant capacity of 140.33 J kg^{-1}, and a high coefficient of performance of 6.12 obtained at 60 kV cm^{-1} make BCZT ceramics potentially useful coolant materials in the development of future eco-friendly solid-state refrigeration technology.

Received 13th July 2020
Accepted 4th August 2020

DOI: 10.1039/d0ra06116f

rsc.li/rsc-advances

1 Introduction

Barium titanate ($BaTiO_3$ denoted as BT) is a bioceramic material without any toxic or volatile elements as compared to lead-based materials like $PbZr_xTi_{1-x}O_3$ (PZT), and its properties can be easily tailored by diverse engineering.[1–3] However, its high dielectric constant decreases sharply around the Curie temperature (T_C) because of the tetragonal-cubic phase transition.[4] Hence, the substantial dielectric, energy storage, and electrocaloric properties can only be observed in a narrow temperature range.[5,6] To overcome this drawback, researchers have focused on systems with a diffuse ferroelectric transition like ferroelectric relaxors due to the broad operating temperature.[7] The doping of $BaTiO_3$ with Ca and Zr demonstrated notable improvements in the electrical and electrocaloric properties due to the enhanced relaxor behavior of BT-based ceramics.[8–12]

In 2009, Liu and Ren[13] reported a Pb-free ceramic with composition $Ba_{0.85}Ca_{0.15}Zr_{0.10}Ti_{0.90}O_3$ (BCZT), having extremely high dielectric constant and piezoelectric properties at the Morphotropic Phase Boundary (MPB). This lead-free ceramic possesses a broad frequency-dependent peak corresponding to the temperature-dependent dielectric susceptibility, lower remnant polarization, and slimmer hysteresis loops due to the relaxor ferroelectric nanodomains, which are essential for realizing extremely high energy densities and efficiencies.[14–17] Moreover, it was reported that BCZT ceramics possess low dielectric loss (tan δ) (1–3%), which is encouraging for obtaining high-efficiency energy storage density.[10,18–21]

BCZT relaxor ferroelectric ceramics have been attracting much attention for energy storage applications and electrocaloric cooling devices owing to their outstanding dielectric and ferroelectric properties.[22,23] Zhan *et al.*[24] achieved an energy storage density of 590 mJ cm^{-3} and storage efficiency (η) of 72.8% in $Ba_{0.95}Ca_{0.05}Zr_{0.30}Ti_{0.70}O_3$ ceramics at 160 kV cm^{-1}. Puli *et al.*[25] examined the energy density properties in the $(1-x)$

[a]*IMED-Lab, Cadi Ayyad University, Marrakesh, 40000, Morocco. E-mail: Zouhair.hanani@edu.uca.ma*
[b]*ICMCB, University of Bordeaux, Pessac, 33600, France*
[c]*Jozef Stefan Institute, Ljubljana, 1000, Slovenia*
[d]*Mohammed VI Polytechnic University, Ben Guerir, 43150, Morocco*
[e]*LPMC, University of Picardy Jules Verne, Amiens, 80039, France*
[f]*Frantsevich Institute for Problems of Materials Science of NASU, Kyiv, 03142, Ukraine*
[g]*Physics Faculty, Southern Federal University, Rostov-on-Don, 344090, Russia*

$BaZr_{0.20}Ti_{0.80}O_3$–$xBa_{0.70}Ca_{0.30}TiO_3$ ($x = 0.10, 0.15, 0.20$) system, and observed enhanced energy storage density and high energy storage efficiency of 680 mJ cm^{-3} and 72.8%, respectively, at $x = 0.15$, by using an electric field of 170 kV cm^{-1}. The thermal-stability of the recovered energy density plays a crucial role in energy storage technologies. Hence, a wide operating temperature and stable W_{rec} are essential in this type of application.[26]

The electrocaloric effect (ECE) in BCZT relaxor ferroelectric ceramics has been widely investigated.[15,27–31] Kaddoussi *et al.*[12] studied the ECE in $Ba_{0.85}Ca_{0.15}Zr_{0.10}Ti_{0.90}O_3$ indirectly using the Maxwell relation at 8 kV cm^{-1}, and found a low electrocaloric temperature change (ΔT) of 0.152 K. Using the same approach, Ben Abdessalem *et al.*[28] obtained $\Delta T = 0.565$ K at 30 kV cm^{-1}. Zhou *et al.*[32] studied the compositional dependence of the electrocaloric effect in lead-free $(1 - x)Ba(Zr_{0.20}Ti_{0.80})O_3$–$x(Ba_{0.70}Ca_{0.30})TiO_3$ ceramics under a moderate electric field of 28 kV cm^{-1}, and reported a high ECE response of 0.56 K at $x = 0.6$. For the advanced evaluation of the electrocaloric efficiency, it was highly recommended that the obtained EC properties like ΔT, ΔS (entropy change) be linked to the total energy density (W_{tot}) of the EC material in question to access the coefficient of performance (COP = input power/output cooling power).[33] Nevertheless, few works have simultaneously studied the energy storage performances and electrocaloric effect (ECE) in BT-based ferroelectric materials. Srikanth *et al.*[34] investigated the electrocaloric effect in $Ba_xSr_{1-x}TiO_3$ ferroelectric ceramics using an indirect approach. ΔT were found to be 0.67, 0.83, and 0.61 K and ΔS was 0.9, 1, and 0.7 J kg^{-1} K^{-1} for $x = 0.7$, 0.8, and 0.9, respectively, under an electric field of 33 kV cm^{-1}. Besides, energy-storage densities of 90, 142, 144 mJ cm^{-3} were observed for $x = 0.7$, 0.8, and 0.9, respectively, which correspond to the estimated COP of 17, 5.47, and 5.68 for $x = 0.7$, 0.8, and 0.9, respectively.[34] We previously reported the synthesis of the BCZT ceramic by surfactant-assisted solvothermal processing.[15] However, only a small total and recovered energy density and electrocaloric response were obtained due to the low applied electric field of 6.6 kV cm^{-1}. It was stated before that the low-temperature hydrothermal processing allowed the possibility to synthesize BCZT ceramics with enhanced dielectric and ferroelectric properties.[35] In this work, the ferroelectric-paraelectric phase transition in the BCZT ceramic was investigated *via* temperature-dependent X-ray diffraction, Raman spectroscopy and dielectric measurements. Field-dependence and the temperature stability of the energy storage performances of the BCZT ceramic were also investigated at 60 kV cm^{-1}. Moreover, the electrocaloric effect in BCZT ceramic was explored *via* an indirect approach following the Maxwell relation, and the ECE performances like the refrigerant capacity (RC)[33] and COP of the BCZT ceramic were examined and compared to lead-free and lead-based materials.

2 Experimental section

$Ba_{0.85}Ca_{0.15}Zr_{0.10}Ti_{0.90}O_3$ (BCZT) powder was elaborated by low-temperature hydrothermal processing at 160 °C for 24 h, followed by sintering at 1250 °C for 10 h. Details about the elaboration and additional characterization of BCZT powder and ceramic can be found in previous reports.[35,36] A transmission electron microscope (TEM, JEOL – ARM 200F Cold FEG TEM/STEM) operating at 200 kV, equipped with a spherical aberration (C_s) probe and image correctors with point resolution 0.12 nm, was used to observe the morphology of the BCZT powder. Thermogravimetric analysis (TGA, Discovery Series TGA 55, TA instruments) was used to characterize the transformations occurring in the BCZT powder from 300 to 1100 K at a heating rate of 10 °C min^{-1} and a nitrogen flow of 40 ml min^{-1}. The crystalline structure and structural change in the BCZT ceramic were examined by X-ray diffraction (XRD, Rigaku SmartLab). The measurements were done in the temperature range 300–400 K at a step angle of 0.02° in the 2θ range from 10 to 80° using Cu-Kα radiation ($\lambda \sim 1.540593$ Å). Raman spectroscopy was also employed to determine the structural property changes in the BCZT ceramic from 300 to 400 K. For this purpose, the BCZT sample was excited using the polarized radiation of an argon laser ($\lambda = 514.5$ nm) and the Raman spectra were recorded using a Renishaw inVia Reflex spectrometer. A well-calibrated Linkam heating–cooling stage with temperature stability of 0.1 K was utilized to control the sample temperature. To compare the spectra obtained at various temperatures, a Bose–Einstein correction was performed. The surface morphology was analyzed using a scanning electron microscope (SEM, Tescan VEGA-3) at a voltage of 10 kV. The dielectric properties of gold-sputtered BCZT pellets in the frequency range of 20 Hz to 1 MHz were measured using a precision LCR meter (HP 4284A, 20 Hz to 1 MHz). The ferroelectric hysteresis loops of the BCZT sample, with a thickness of 340 μm, were measured using a ferroelectric test system (AiXACCT, TF Analyzer 2000) equipped with a high-voltage amplifier (TREK model 609E-6) in a silicone oil bath. The hysteresis loops were obtained by using triangular voltage waveforms at a frequency of 10 Hz at room temperature in different electric fields (10–60 kV cm^{-1}), and in the temperature range of 300–400 K with a 5 K step for heating cycles at 60 kV cm^{-1}. The ECE response was calculated from the recorded *P*–*E* hysteresis loops at 10 Hz by using the indirect Maxwell approach.

3 Results and discussion

3.1. Structural properties

A TEM image of the BCZT powder and the particle size distribution are depicted in Fig. 1a and b, respectively. Near-spherical BCZT nanoparticles with an average particle size of 94 nm were formed, as seen in the inset of Fig. 1b. The growth mechanism of the BCZT powder was reported in ref. 37 The thermal evolution of the as-prepared BCZT powder *via* low-temperature hydrothermal processing is shown in Fig. 1c. Two consecutive weight losses at temperatures in the 300–520 K range are due to dehydration and dehydroxylation phenomena. The weight loss in the range 520–770 K is associated with the thermal decomposition of different organic compounds, and after 770 K, the weight loss remained constant. More interestingly, the absence of weight loss above 770 K was attributed to the formation and crystallization of BCZT perovskite phase, as reported previously,[27,38–42] and the low total weight loss (6.12%) in the BCZT

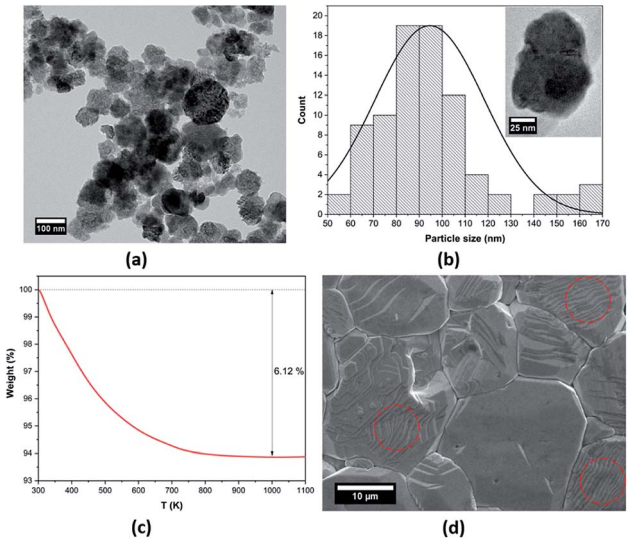

Fig. 1 (a) TEM image, (b) grain size distribution (a single BCZT nanoparticle is shown in the inset), (c) TGA curve of the BCZT powder, and (d) SEM micrograph of the BCZT sintered ceramic.

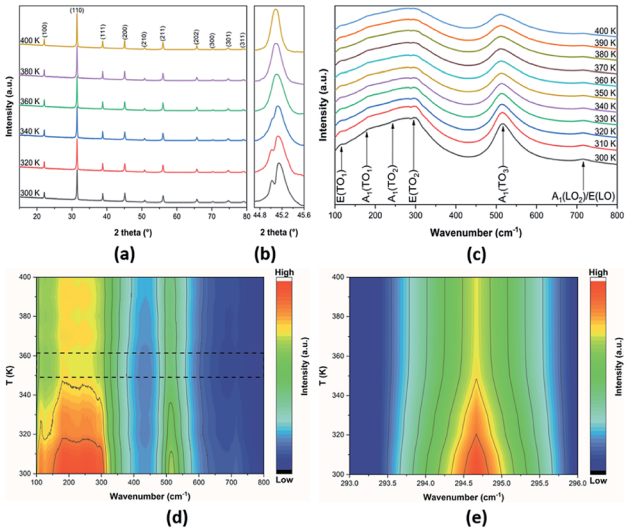

Fig. 2 (a) Temperature-dependence of the XRD pattern, (b) enlarged peak splitting around 2θ of $\sim 45°$, (c) temperature-dependence and (d) 2D colour map of the Raman spectra, and (e) 2D colour map of the $E(TO_2)$ Raman mode of the BCZT ceramic.

powder indicates that the BCZT perovskite phase was formed at low-temperature (160 °C).[37] Therefore, the synthesis temperature of BCZT powders can be decreased to a low temperature of 160 °C, which is about 1200 °C lower when compared with the solid-state reaction, and 840 °C lower when compared with sol–gel methods.[35] This temperature decrease is important in the large-scale industrial production of ferroelectric materials. Fig. 1d provides a typical SEM image of the microstructure of BCZT sintered ceramic at 1250 °C for 10 h. Coarse and flattened grains with an average grain size of 22.1 μm (determined by the intercept method) and well-defined grain boundaries, were observed in the BCZT ceramic. Interestingly, as highlighted with dashed circles, the domain patterns of parallel stripes with average domain sizes (150–600 nm) were seen inside the grains.

The structural changes in the BCZT sintered ceramic were examined *via* the temperature dependence of XRD and Raman spectroscopy. Fig. 2a displays the temperature-dependent XRD patterns of the BCZT ceramic in the temperature range between 300 and 400 K. Pure perovskite structures were formed without any secondary phases, and all peaks were indexed based on the standard $BaTiO_3$ pattern (JCPDS card no. 96-901-4669). At 300 K, the BCZT ceramic exhibited tetragonal symmetry with space group *P4mm*, due to the peak splitting at around $2\theta \sim 45°$ (Fig. 2b).[13,43]

To gain insight into the structural changes in the BCZT ceramic with increasing temperature, the thermal evolution of the peak around $2\theta \sim 45°$ was followed by *in situ* XRD (Fig. 2b). On increasing the temperature, the peak at around $2\theta \sim 45°$ tends to merge into a single peak between 340 and 360 K due to the tetragonal-cubic phase transition,[43] and with a further increase in temperature, this peak became sharper. It is worth mentioning that with increasing temperature, all peaks shifted toward lower 2θ, due to the unit cell expansion and the decreasing of the tetragonal phase.[12] Besides, Raman spectroscopy is used to have an idea about this structural change in BCZT sintered ceramic in the temperature range 300–400 K (Fig. 2c). The observed Raman peaks around 115, 180, 245, 294, 517, and 716 cm^{-1} correspond to $E(TO_1)$, $A_1(TO_1)$, $A_1(TO_2)$, $E(TO_2)$, $A_1(TO_3)$, and $A_1(LO_2)/E(LO)$, respectively. These peaks are characteristics of perovskite oxides.[44,45] With increasing temperature, the peak position and the intensity of the Raman modes present a decreasing trend, alongside with Raman modes broadening, which is similar to other ferroelectric materials.[44,46] A 2D colour map of Raman spectra of BCZT ceramic is illustrated in Fig. 2d.

It was observed that the low-temperature data had a much greater signal and lower background as compared to the high-temperature data. Note that the changes in the contour plots between 349 and 361 K (marked by the dashed rectangles) can be attributed to structural changes in the BCZT ceramic. It was stated that the $E(TO_2)$ mode is associated with the tetragonal phase transition.[47] In order to reveal the origin of the detected structural change in the BCZT ceramic, the wavenumbers around 292–296 cm^{-1} and temperature between 300 and 400 K were plotted using a 2D colour map as shown in Fig. 2e. It was observed that the intensity of the $E(TO_2)$ mode decreased with increasing temperature, and an abrupt intensity change in this mode occurred at 355 K due to the structural change from ferroelectric (tetragonal) to paraelectric (cubic).[15,48]

3.2. Dielectric properties

The room-temperature dielectric properties of the BCZT ceramic sintered at 1250 °C for 10 h are depicted in Fig. 3a. The dielectric constant (ε_r) and the dielectric loss (tan δ) of the BCZT ceramic decreased with the increasing frequency. At 1 kHz, ε_r and tan δ were found to be 5000 and 0.029, respectively, these properties were enhanced as compared to some reported works

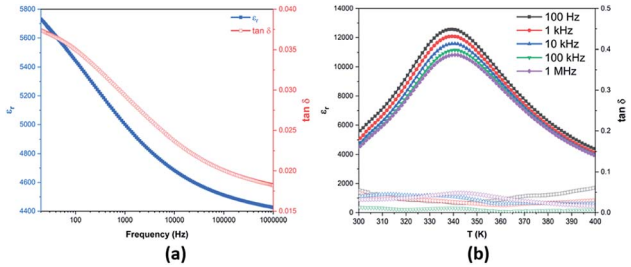

Fig. 3 (a) Room-temperature frequency dependence and (b) temperature-dependence of the dielectric properties of the BCZT ceramic.

in the literature using BCZT ceramics with the same composition.[49–52] Fig. 3b displays the temperature dependence of ε_r and tan δ of the BCZT ceramic at different frequencies in the temperature range of 300–400 K. The broad peak at around 340 K is associated with the tetragonal-cubic phase transition.[10,53,54] The low T_C observed in the BCZT ceramic is related to the elaboration method, calcination, sintering temperature and dwell time.[55] Hunpratub *et al.*[56] elaborated a BCZT ceramic with the same composition using the hydrothermal reaction at different sintering temperatures and found T_C ranging between 333 and 343 K. These results corroborate those obtained by XRD and Raman analyses, assuming the structural change from ferroelectric (tetragonal) to paraelectric (cubic) in the BCZT ceramic.

3.3. Energy storage in the BCZT ceramic

3.3.1. Room-temperature energy storage. Fig. 4 schematizes the areas of the recovered energy (W_{rec}, green area) and loss energy (W_{loss}, red area) in a *P*–*E* hysteresis loop. These, including the W_{tot}, and η, can be estimated using eqn (1)–(3):

$$W_{tot} = \int_0^{P_{max}} E dP, \quad (1)$$

$$W_{rec} = \int_{P_r}^{P_{max}} E dP, \quad (2)$$

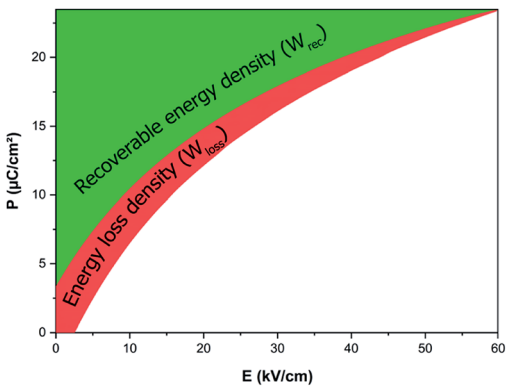

Fig. 4 Schematic illustration of the calculation of W_{rec} and W_{loss} parameters.

$$\eta\ (\%) = \frac{W_{rec}}{W_{tot}} \times 100 = \frac{W_{rec}}{W_{rec} + W_{loss}} \times 100, \quad (3)$$

where W_{tot}, W_{rec}, W_{loss}, and η are the total, recoverable and loss energy densities as well as energy efficiency, respectively, while *P*, P_r, P_{max}, *E*, represent the polarization, remnant polarization, maximum polarization, and electric field, respectively.

Room-temperature *P*–*E* hysteresis loops of the BCZT ceramic at various electric fields from 10 to 60 kV cm^{-1} are shown in Fig. 5a. It was observed that the BCZT ceramic exhibited enhanced ferroelectric properties. The maximal polarization (P_{max}), remnant polarization (P_r), and coercive field (E_c) increased on increasing the applied electric field. At 60 kV cm^{-1}, the values of P_{max}, P_r, and E_c reached 27.21 μC cm^{-2}, 8.59 μC cm^{-2} and 4.10 kV cm^{-1}, respectively. It should be noted that the hysteresis loops were not fully saturated at 60 kV cm^{-1}; however, the thickness of the sample prevented us from further increasing the electric field.

From the first two equations, the increasing applied electric field boosted the obtained energy storage density. The room-temperature electric field-dependence of the energy storage properties of the BCZT ceramic is shown in Fig. 5b. As desired, after increasing the applied electric field from 10 to 60 kV cm^{-1}, the linear behavior of the W_{tot} and W_{rec} was observed, where, W_{tot} and W_{rec} increased from 44.1 and 31.4 mJ cm^{-3} to 546.1 and 367.2 mJ cm^{-3}, respectively. However, η dropped from 71.2% to 67.2%, respectively. At 60 kV cm^{-1}, Xu *et al.*[26] and Puli *et al.*[57] obtained W_{rec} of 121.6 mJ cm^{-3} (η = 51.3%) and 280 mJ cm^{-3} (η = 58.3%), respectively. These values are lower than those obtained in the BCZT ceramic (W_{rec} = 367.2 mJ cm^{-3}, η = 67.2%).

Table 1 compares the energy storage properties of the BCZT ceramic with other lead-free ceramics reported in the literature. Under the high electric field of 160 kV cm^{-1}, Zhan *et al.*[24] achieved a recovered energy density of 590 mJ cm^{-3} and storage efficiency of 72.8% in the $Ba_{0.95}Ca_{0.05}Zr_{0.3}Ti_{0.7}O_3$ ceramic. Meanwhile, using an electric field of 170 kV cm^{-1}, Puli *et al.*[25] observed a recovered energy density and energy storage efficiency of 680 mJ cm^{-3} and 72%, respectively, in the $0.85BaZr_{0.2}Ti_{0.8}O_3$–$0.15Ba_{0.7}Ca_{0.3}TiO_3$ system. In a recent study, Puli *et al.*[57] observed an energy storage density of 1.33 J cm^{-3} at 106 kV cm^{-1} but with a reduced energy efficiency of 52.3% in the $Ba_{0.85}Ca_{0.15}Zr_{0.10}Ti_{0.90}O_3$ ceramic. It was stated before that the non-saturated *P*–*E* loops in the BCZT ceramic could help to

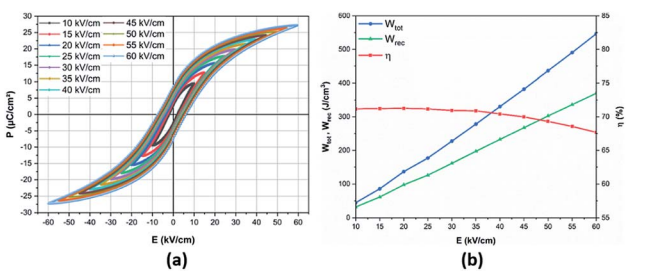

Fig. 5 (a) Room-temperature electric field-dependence of *P*–*E* loops; (b) energy storage performances in the BCZT ceramic.

Table 1 Comparison of the energy storage properties of BCZT ceramics with other lead-free ceramics reported in the literature

Ceramic	W_{tot} (mJ cm^{-3})	W_{rec} (mJ cm^{-3})	η (%)	E (kV cm^{-1})	T (K)	Ref.
$Ba_{0.85}Ca_{0.15}Zr_{0.10}Ti_{0.90}O_3$	546.1	367.2	67.2	60	300	This work
$Ba_{0.85}Ca_{0.15}Zr_{0.10}Ti_{0.90}O_3$	535.3	398.5	74.4	60	340	This work
$Ba_{0.85}Ca_{0.15}Zr_{0.10}Ti_{0.90}O_3$	526.6	414.1	78.6	60	380	This work
$Ba_{0.85}Ca_{0.15}Zr_{0.10}Ti_{0.90}O_3$	436.3	302.4	69.3	50	300	This work
$Ba_{0.85}Ca_{0.15}Zr_{0.10}Ti_{0.90}O_3$	278.3	197.3	70.9	35	300	This work
$Ba_{0.85}Ca_{0.15}Zr_{0.10}Ti_{0.90}O_3$	136.7	97.4	71.3	20	300	This work
$Ba_{0.85}Ca_{0.15}Zr_{0.10}Ti_{0.90}O_3$	44.1	31.4	71.2	10	300	This work
$Ba_{0.85}Ca_{0.15}Zr_{0.10}Ti_{0.90}O_3$	236.4	121.6	51.3	60	RT	26
$Ba_{0.85}Ca_{0.15}Zr_{0.10}Ti_{0.90}O_3$	480.3	280	58.3	60	RT	57
$Ba_{0.85}Ca_{0.15}Zr_{0.10}Ti_{0.90}O_3$	1330	695.6	52.3	106	RT	57
$0.6BaZr_{0.20}Ti_{0.80}O_3$–$0.4Ba_{0.70}Ca_{0.30}TiO_3$	207	149	72	35	303	63
$Ba_{0.85}Ca_{0.15}Zr_{0.10}Ti_{0.90}O_3$ (32.84 μm)	113.8	38.6	33.9	20	298	64
$Ba_{0.85}Ca_{0.15}Zr_{0.10}Ti_{0.90}O_3$ (32.84 μm)	90.2	71.2	78.9	20	373	64
$Ba_{0.85}Ca_{0.15}Zr_{0.10}Ti_{0.90}O_3$ (44.37 μm)	98.1	36.4	37.1	20	298	64
$Ba_{0.85}Ca_{0.15}Zr_{0.10}Ti_{0.90}O_3$ (44.37 μm)	81.1	69.6	85.8	20	373	64
$Ba_{0.95}Ca_{0.05}Zr_{0.30}Ti_{0.70}O_3$	810.4	590	72.8	160	RT	24
$Ba_{0.95}Ca_{0.05}Zr_{0.20}Ti_{0.80}O_3$	569.4	410	72	120	RT	65
$0.85BaZr_{0.20}Ti_{0.80}O_3$–$0.15Ba_{0.70}Ca_{0.30}TiO_3$	940	680	72	170	RT	25
$Ba_{0.975}La_{0.017}(Zr_{0.05}Ti_{0.90})Sn_{0.05}O_3$	108.3	65	60	12	300	66
$BaTi_{0.89}Sn_{0.11}O_3$	92.7	84.4	91.04	25	333	67
$BaTiO_3$	1594	450	28.23	110	RT	68
$BaZr_{0.05}Ti_{0.95}O_3$	302	218	72	50	RT	69
$0.90(0.92Bi_{0.50}Na_{0.50}TiO_3$–$0.08BaTiO_3)$–$0.10NaNbO_3$	1082	710	65.6	70	298	61
$0.90(0.92Bi_{0.50}Na_{0.50}TiO_3$–$0.08BaTiO_3)$–$0.10NaNbO_3$	954.1	790	82.8	70	373	61
$Bi_{0.48}La_{0.02}Na_{0.40}K_{0.10}Ti_{0.98}Zr_{0.02}O_3$	1033	630	61	60	298	62
$Bi_{0.48}La_{0.02}Na_{0.40}K_{0.10}Ti_{0.98}Zr_{0.02}O_3$	783.1	650	83	60	348	62
$Bi_{0.48}La_{0.02}Na_{0.40}K_{0.10}Ti_{0.98}Zr_{0.02}O_3$	755.5	680	90	60	298	62

further increase the applied electric field, hence, enhancing the energy density. However, to avoid the electric breakdown at high temperature, the electric field was kept at 60 kV cm^{-1}.

3.3.2. Temperature-dependence of the energy storage. It is well-known that excellent temperature stability in a wide operating temperature is a vital factor for the practical application of energy storage capacitors. Therefore, the enhancement of dielectric and ferroelectric properties over a wide operating temperature is the priority research consideration.[26] For this purpose, *P*–*E* hysteresis loops of the BCZT ceramic were obtained from 300 to 400 K and plotted in Fig. 6a. As the temperature increased, the *P*–*E* loops became slimmer, accompanied by the continuous decrease in P_r and P_{max}, due to the shift in the ferroelectric domain direction. Above T_C, the *P*–*E* loops do not show strictly linear behavior, which is characteristic of the pure paraelectric phase. In contrast, very slim loops appeared, corresponding to the existence of ferroelectric clusters or residual polar nanoregions (PNR),[58–60] often attributed to the relaxor behavior.[29] The temperature-dependence of the energy storage performances of the BCZT ceramic at 60 kV cm^{-1} is presented in Fig. 6b. It was observed that W_{rec} and η increased gradually with temperature to reach a maximum of 414.1 mJ cm^{-3} and 78.6%, respectively, at 380 K, then decreased. Furthermore, the variation rate of W_{rec} or energy-storage variation (ESV) in the temperature range of 300–400 K was calculated by the following equation:[61,62]

$$\frac{\Delta W_{rec,T}}{W_{rec,300\ K}} = \left|\frac{W_{rec,T} - W_{rec,300\ K}}{W_{rec,300\ K}}\right|, \quad (4)$$

where $W_{rec,T}$ is the W_{rec} value at a given temperature, and $\Delta W_{rec,T}$ is the difference of $W_{rec,T}$ and $W_{rec,300\ K}$.

The temperature-dependence of $\Delta W_{rec,T}/W_{rec,300\ K}$ values in BCZT ceramics is depicted in Fig. 7. It was observed that $\Delta W_{rec,T}/W_{rec,300\ K}$ of BCZT ceramics is always less than 12.7% ($W_{rec} \sim$ 367.2–414.1 mJ cm^{-3}) in the temperature range from 300 to 400 K, indicating the excellent energy storage capabilities in a wide temperature range. The energy-storage variation in BCZT ceramics is lower than that reported by Jayakrishnan *et al.*[63] in $0.6BaZr_{0.20}Ti_{0.80}O_3$–$0.4Ba_{0.70}Ca_{0.30}TiO_3$, where W_{rec} at 25 kV cm^{-1} dropped from 121, 115 to 65 mJ cm^{-3}, at 303, 323 and 363 K, respectively, corresponding to $\Delta W_{rec,T}/W_{rec,300\ K}$ of 46.3%. Furthermore, the obtained value of the variation in the recovered energy density was also lower than that found by Xu

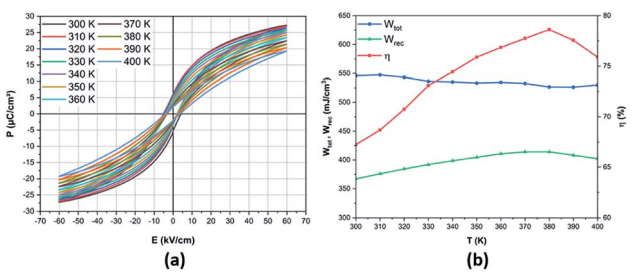

Fig. 6 Temperature-dependence of (a) *P*–*E* loops; (b) energy storage performances of the BCZT ceramic at 60 kV cm^{-1}.

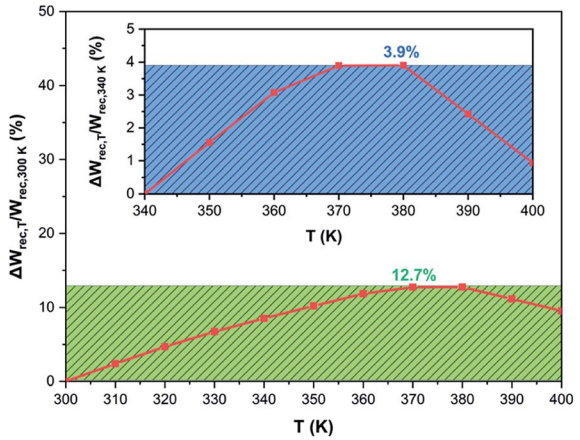

Fig. 7 The thermal stability of $\Delta W_{rec,T}/W_{rec,300\ K}$ and $\Delta W_{rec,T}/W_{rec,340\ K}$ (inset) of the BCZT ceramic at 60 kV cm^{-1}.

et al.[26] in the BCZT–0.5 wt% MgO ceramic (14.18%). Despite the enhanced energy efficiency in BCZT ceramics with different grain sizes found by Cai *et al.*[64] at 20 kV cm^{-1}, the high variation in the recovered energy density was observed in the temperature range of 298 to 393 K (84.4% and 91.2 for BCZT with grain sizes of 32.84 and 44.37 μm, respectively). Besides, Liu *et al.*[70] obtained an ESV value of 15% in the temperature range of 298–373 K in the lead-based $Pb_{0.97}La_{0.02}(Zr_{0.58}Sn_{0.335}Ti_{0.085})O_3$ ceramic, which is higher than that obtained in the BCZT ceramic. A similar energy-storage variation was obtained by Xu *et al.*[61] in the $0.90(0.92Bi_{0.50}Na_{0.50}TiO_3–0.08BaTiO_3)–0.10NaNbO_3$ ceramic at 70 kV cm^{-1} in the temperature range of 298–423 K.

In the case of a high-temperature range, the temperature variation in W_{rec} values was estimated within the temperature range of 340–400 K by eqn (5), according to Malik *et al.*,[71]

$$\frac{\Delta W_{rec,T}}{W_{rec,340\ K}} = \left|\frac{W_{rec,T} - W_{rec,340\ K}}{W_{rec,340\ K}}\right|, \quad (5)$$

where $\Delta W_{rec,T}$ is the difference of $W_{rec,T}$ (T above 340 K) and $W_{rec,340\ K}$.

A plot of $\Delta W_{rec,T}/W_{rec,340\ K}$ values as a function of temperature in the BCZT ceramic is displayed in the inset of Fig. 7. The temperature variation in the energy storage density values of the BCZT ceramic was estimated to be 3.9% (398.5–414.1 mJ cm^{-3}). These values are considered to be excellent as compared with many lead-free ferroelectric ceramics.[26,62,63,71,72]

For instance, Butnoi *et al.*[62] found an ESV ratio of 4.6% in $Bi_{0.48}La_{0.02}Na_{0.40}K_{0.10}Ti_{0.98}Zr_{0.02}O_3$ ceramics in the temperature range of 348–423 K. The high energy storage density in relaxor ferroelectric ceramics is due to the diffuse phase transition.[73] Consequently, ferroelectricity can be detected in a wide temperature range in relaxor ferroelectrics, which significantly reduces ESV, thus keeping energy storage enhanced in a wide temperature range.[15] It is worth recalling that the BCZT powder was elaborated at 160 °C for 24 h in contrast to other lead-free-based powders reported in the literature, including BCZT, which request an inevitable calcination step at high temperature.[25,26,57,61–65,69] Hence, the hydrothermal method has better advantages in the elaboration of BCZT ceramics at lower sintering temperatures and with outstanding and thermally-stable energy storage performances.

3.4. The electrocaloric effect in BCZT ceramics

The electrocaloric effect (ECE) under higher electric fields in BCZT relaxor ferroelectric ceramics was evaluated by using the indirect approach based on the Maxwell relation.[33] The indirect method is based on calculating the ECE from the measured ferroelectric order parameter P (T, E) obtained from the temperature-dependence of the P–E hysteresis loops, as shown in Fig. 8a. A fifth-order polynomial fitting of the upper polarization branches was performed at every fixed applied electric field. It can be seen that P gradually diminished with increasing the temperature. The isothermal entropy change (ΔS) and the electrocaloric temperature change (ΔT) were calculated from eqn (7) and (8),

$$\Delta S = \int_{E_1}^{E_2} \left(\frac{\partial P}{\partial T}\right)_E dE, \quad (6)$$

$$\Delta T = -\int_{E_1}^{E_2} \frac{T}{\rho C_p} \left(\frac{\partial P}{\partial T}\right)_E dE. \quad (7)$$

Here, ρ and C_p are the mass density and the specific heat of the sample, respectively. E_1 and E_2 denote the initial and the final electric fields, respectively. The value of C_p (0.4 J g^{-1} K^{-1}) was taken from ref. 32.

The thermal evolution of the reversible electrocaloric temperature change (ΔT) and the corresponding entropy change (ΔS) under different applied electric fields in the BCZT ceramic are shown in Fig. 8b and c, respectively. ΔT and ΔS increased with increasing the applied electric field, and the temperature at which the maximum was obtained shifted toward higher temperatures. This indicates that the T_C of BCZT ceramic shifted to higher temperatures under a higher electric field.[74] At 60 kV cm^{-1}, a large ΔT and ΔS of 1.479 K and 1.613 J kg^{-1} K^{-1} were

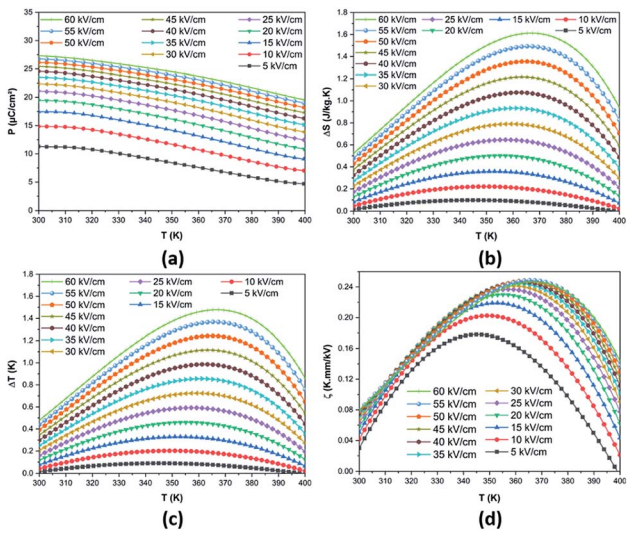

Fig. 8 Temperature-dependence of (a) P, (b) ΔS, (c) ΔT and (d) ζ at various applied electric fields in the BCZT ceramic.

found in the BCZT ceramic in the vicinity of the tetragonal-cubic phase transition at 367 K, respectively. Comparable values of ΔS = 1.78 and 1.53 J kg^{-1} K^{-1} were reported by Xin *et al.*[6] at 70 kV cm^{-1} in $Ba_{0.9}Ca_{0.1}Zr_{0.05}Ti_{0.95}O_3$ and $Ba_{0.9}Ca_{0.1}Zr_{0.1}Ti_{0.9}O_3$ ceramics, respectively. Fig. 8d plots the electrocaloric responsivity $\zeta = \Delta T/\Delta E$ as a function of temperature and applied electric field. It was observed that the temperature of the ECE responsivity peak and its magnitude initially increased with increasing the applied electric field then gradually became stable at higher fields. The ECE responsivity saturation could be ascribed to the diffused phase transition and the relaxor behavior in the BCZT ceramic, as observed by Xin *et al.*[6]

Table 2 compares the EC responses (ΔT and ζ) in BCZT ceramics with previously published results on lead-free ceramics obtained *via* the indirect approach under different applied electric fields. At a low electric field of 8 kV cm^{-1}, our ceramics exhibited comparable ECE properties (ΔT = 0.155 K and ζ = 0.194 K mm kV^{-1} at 347 K) to those found in $Ba_{0.85}Ca_{0.15}Zr_{0.10}Ti_{0.90}O_3$ ceramics synthesized *via* the solid-state method (ΔT = 0.152 K and ζ = 0.19 K mm kV^{-1} at 343 K) by Kaddoussi *et al.*[12] Hanani *et al.*[27] reported ECE properties (ΔT = 0.492 K and ζ = 0.289 K mm kV^{-1} at 360 K) at a low electric field of 17 kV cm^{-1} in the rod-like $Ba_{0.85}Ca_{0.15}Zr_{0.10}Ti_{0.90}O_3$ ceramic, elaborated by a surfactant-assisted solvothermal route, which are just slightly higher than the present results (ΔT = 0.38 K and ζ = 0.223 K mm kV^{-1} at 353 K). Nevertheless, the ECE of our sample at 40 kV cm^{-1} (ΔT = 0.986 K and ζ = 0.245 K mm kV^{-1} at 363 K) is larger than that obtained for the $Ba_{0.65}Sr_{0.35}TiO_3$ ceramic by a spark plasma sintering process (ΔT = 0.328 K and ζ = 0.164 K mm kV^{-1} at 303 K) as stated by Liu *et al.*[75] Furthermore, Patel *et al.*[76] elaborated the $Ba_{0.85}Ca_{0.075}Sr_{0.075}Ti_{0.90}Zr_{0.10}O_3$ ceramic by the conventional solid-state method, revealing that the ECE response reached high values of 1.6 K and 0.405 K mm kV^{-1} for ΔT and ζ, respectively, under 39.5 kV cm^{-1} at room temperature. Smail *et al.*[66] reported ECE properties (ΔT = 0.24 K and ζ = 0.20 K mm kV^{-1} at 338 K) at a low electric field of 12 kV cm^{-1} in $Ba_{0.975}La_{0.017}(Zr_{0.05}Ti_{0.90})Sn_{0.05}O_3$ ceramics synthesized by solid-state reaction. These differences can be attributed to the synthesis conditions (such as calcination and sintering), chemical doping, grain shape, the number of the coexisting phases as well as the applied external electric field.

The applied electric field-dependence of ΔT and the EC responsivity ζ at the peak temperature are presented in Fig. 9a. ΔT increased with the increasing electric field. In contrast, ζ increased rapidly at low electric fields, then became nearly saturated above 40 kV cm^{-1}, and finally started decreasing above 55 kV cm^{-1}. The EC responsivity ζ, therefore, exhibited a maximum as predicted by theory and confirmed by experimental results in relaxor ferroelectrics.[77,78]

For practical applications, the temperature range (T_{span}) in which a large ECE can be maintained is also critical. Here, T_{span} was introduced as the full width at half maximum (FWHM) of the ECE peak at 60 kV cm^{-1}.[82,83] The T_{span} value of 87 K was found in the BCZT ceramic, indicating that the BCZT ceramic can maintain a high EC response over a relatively broad temperature range as compared to other materials.[82,84–86] The suitability of the electrocaloric material for application in new cooling technologies is typically evaluated by a parameter similar to refrigerant capacity, RC = $\Delta S \times \delta T_{FWHM} = \Delta S \times T_{span}$.[33,83,87,88] This parameter was estimated to be 140.33 J kg^{-1} at 60 kV cm^{-1} in the BCZT ceramic. The obtained value is higher as compared to many other lead-free ceramics.[74,84] Another important criterion in evaluating the efficiency of an electrocaloric material is the coefficient of performance (COP) as defined by eqn (8),[89,90] where Q is the isothermal heat.

$$\mathrm{COP} = \frac{|Q|}{|W_{tot}|} = \frac{|T\Delta S|}{|W_{tot}|}, \quad (8)$$

Table 2 Comparison of the electrocaloric properties of BCZT ceramics with other lead-free ceramics reported in the literature using the indirect method

Ceramic	ΔT (K)	ΔE (kV cm^{-1})	T (K)	ζ (K mm kV^{-1})	Ref.
$Ba_{0.85}Ca_{0.15}Zr_{0.10}Ti_{0.90}O_3$	1.479	60	367	0.246	This study
$Ba_{0.85}Ca_{0.15}Zr_{0.10}Ti_{0.90}O_3$	0.986	40	363	0.246	This study
$Ba_{0.85}Ca_{0.15}Zr_{0.10}Ti_{0.90}O_3$	0.459	20	355	0.229	This study
$Ba_{0.85}Ca_{0.15}Zr_{0.10}Ti_{0.90}O_3$	0.380	17	353	0.223	This study
$Ba_{0.85}Ca_{0.15}Zr_{0.10}Ti_{0.90}O_3$	0.328	15	353	0.218	This study
$Ba_{0.85}Ca_{0.15}Zr_{0.10}Ti_{0.90}O_3$	0.155	8	347	0.194	This study
$Ba_{0.85}Ca_{0.15}Zr_{0.10}Ti_{0.90}O_3$	0.492	17	360	0.289	27
$Ba_{0.85}Ca_{0.15}Zr_{0.10}Ti_{0.90}O_3$	0.4	21.5	370	0.186	3
$Ba_{0.85}Ca_{0.15}Zr_{0.10}Ti_{0.90}O_3$	0.152	8	373	0.19	12
$Ba_{0.90}Ca_{0.10}Zr_{0.05}Ti_{0.95}O_3$	0.465	25	392	0.186	28
$Ba_{0.91}Ca_{0.09}Zr_{0.14}Ti_{0.86}O_3$	0.3	20	328	0.150	79
$Ba_{0.92}Ca_{0.08}Zr_{0.05}Ti_{0.95}O_3$	0.38	15	410	0.253	80
0.6BZT–0.4BCT	0.58	28	398	0.21	32
BZT–30BCT	0.30	20	333	0.15	79
$Ba_{0.975}La_{0.017}(Zr_{0.05}Ti_{0.90})Sn_{0.05}O_3$	0.24	12	338	0.20	66
$BaTi_{0.89}Sn_{0.11}O_3$	0.71	25	325	0.284	67
$Ba_{0.65}Sr_{0.35}TiO_3$	0.83	40	303	0.21	75
$Ba_{0.85}Sr_{0.15}Ti_{0.9}Zr_{0.1}O_3$	2.4	37	303	0.65	81
$Ba_{0.85}Ca_{0.075}Sr_{0.075}Ti_{0.90}Zr_{0.10}O_3$	1.60	39.5	303	0.405	76

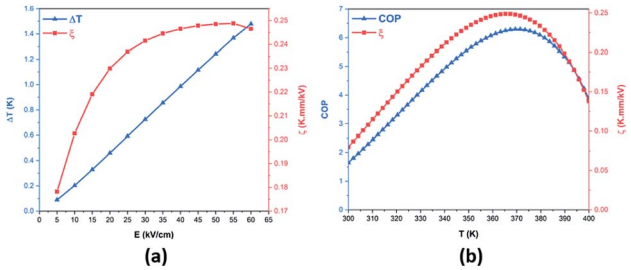

Fig. 9 (a) Electric field-dependence of ΔT and ζ at the temperature of peak response; (b) thermal evolution of the COP and ζ in the BCZT ceramic at 55 kV cm^{-1}.

It was established before that ζ exhibited a maximum at 55 kV cm^{-1} (Fig. 9a); hence, the COP value was determined at 55 kV cm^{-1}. The COP of the BCZT ceramic reached a maximum of 6.29 at 365 K and 55 kV cm^{-1} as shown in Fig. 9b. The obtained value is higher than those reported in several works in lead-free materials[89,91–94] and some lead-based materials.[90,95–98] For instance, Hao *et al.*[97] found a COP value of 2.9 in $Pb_{0.97}La_{0.02}Zr_{0.87}Sn_{0.08}Ti_{0.07}O_3$ thick film.[97] The obtained high values of ΔT, ΔS, ζ, RC and COP, and the wide operating temperature range make BCZT ceramics, elaborated by the low-temperature hydrothermal method, a promising candidate for eco-friendly electrocaloric cooling technologies.

4 Conclusions

In conclusion, the temperature-dependent structural, dielectric, energy storage and EC properties in the lead-free BCZT ceramic were elaborated by low-temperature hydrothermal processing and systematically studied. Enhanced dielectric properties were found (at room temperature, $\varepsilon_r = 5000$ and $\tan\delta = 0.029$). The BCZT ceramic exhibited a large W_{rec} of 414.1 mJ cm^{-3} at 380 K, with an energy efficiency of 78.6%. In contrast to other $BaTiO_3$-based lead-free ceramics, the BCZT ceramic exhibits the lower temperature variation of the recovered energy density of 12.7% and 3.9% in the temperature ranges of 300–400 K and 340–400 K, respectively. Besides, the existence of the large electrocaloric effect in the BCZT ceramic was demonstrated. At 60 kV cm^{-1}, a maximum ΔT and ΔS of 1.479 K and 1.613 J kg^{-1} K^{-1} were observed at 367 K, whereas, the maximum value of the EC responsivity $\zeta = 0.25$ K mm kV^{-1} was found at 55 kV cm^{-1}. The corresponding COP maximum value of 6.29 was calculated at 55 kV cm^{-1}. The temperature range (T_{span}) in which a large ECE was maintained, and refrigerant capacity RC, were estimated to be 87 K and 140.33 J kg^{-1}, respectively, at 60 kV cm^{-1}. Therefore, the obtained excellent electrocaloric properties make the BCZT ceramic a potential candidate for solid-state electrocaloric cooling technologies.

Statement of contributions

Z. H., D. M. and M. A. designed the research. Z. H. and S. M. performed the experiments, analyzed the results and drafted the manuscript. A. B. carried out the temperature dependence of the *P–E* measurements. L. M. provided facilities for TGA analyses; M. M. provided facilities for Raman spectroscopy; B. R., A. V. R., I. A. L., and Z. K. reviewed and edited the drafted manuscript and provided discussion of the energy storage and electrocaloric properties sections; M. M., I. A. L., B. R., Z. K. and M. G. coordinated and financed the project. D. M., M. A. and M. G. supervised the overall project. The manuscript was written through contributions of all the authors.

Conflicts of interest

There are no conflicts to declare.

Acknowledgements

The authors gratefully acknowledge the generous financial support of CNRST Priority Program PPR 15/2015 and the European Union Horizon 2020 Research and Innovation actions MSCA-RISE-ENGIMA (No. 778072) and MSCA-RISE-MELON (No. 872631). Z. K. and B. R. acknowledge Slovenian Research Agency grant J1-9147 and program P1-0125.

References

1 I. Coondoo, N. Panwar, H. Amorín, M. Alguero and A. L. Kholkin, *J. Appl. Phys.*, 2013, **113**, 214107.
2 J. Gao, X. Hu, Y. Wang, Y. Liu, L. Zhang, X. Ke, L. Zhong, H. Zhao and X. Ren, *Acta Mater.*, 2017, **125**, 177–186.
3 S. Patel, P. Sharma and R. Vaish, *Phase Transitions*, 2016, **89**, 1062–1073.
4 F. Wang, W. Li, H. Jiang, M. Xue, J. Lu and J. Yao, *J. Appl. Phys.*, 2010, **107**, 043528.
5 K. Uchino and S. Nomura, *Ferroelectr., Lett. Sect.*, 1982, **44**, 55–61.
6 X. Nie, S. Yan, S. Guo, F. Cao, C. Yao, C. Mao, X. Dong and G. Wang, *J. Am. Ceram. Soc.*, 2017, **100**, 5202–5210.
7 J. Wu, in *Advances in Lead-Free Piezoelectric Materials*, Springer Singapore, Singapore, 2018, pp. 247–299.
8 M. A. Rafiq, M. N. Rafiq and K. Venkata Saravanan, *Ceram. Int.*, 2015, **41**, 11436–11444.
9 S. Liu, S. Xue, W. Zhang and J. Zhai, *Ceram. Int.*, 2014, **40**, 15633–15640.
10 Z. Hanani, D. Mezzane, M. Amjoud, S. Fourcade, A. G. Razumnaya, I. A. Luk'yanchuk and M. Gouné, *Superlattices Microstruct.*, 2019, **127**, 109–117.
11 H. Kaddoussi, A. Lahmar, Y. Gagou, B. Asbani, J. L. Dellis, G. Cordoyiannis, B. Allouche, H. Khemakhem, Z. Kutnjak and M. El Marssi, *J. Alloys Compd.*, 2016, **667**, 198–203.
12 H. Kaddoussi, A. Lahmar, Y. Gagou, B. Manoun, J. N. Chotard, J. L. Dellis, Z. Kutnjak, H. Khemakhem, B. Elouadi and M. El Marssi, *J. Alloys Compd.*, 2017, **713**, 164–179.
13 W. Liu and X. Ren, *Phys. Rev. Lett.*, 2009, **103**, 257602.
14 M. D. Nguyen, E. P. Houwman, M. Dekkers, C. T. Q. Nguyen, H. N. Vu and G. Rijnders, *APL Mater.*, 2016, **4**, 080701.
15 Z. Hanani, D. Mezzane, M. Amjoud, A. G. Razumnaya, S. Fourcade, Y. Gagou, K. Hoummada, M. El Marssi and M. Gouné, *J. Mater. Sci.: Mater. Electron.*, 2019, **30**, 6430–6438.

16 S. Patel, A. Chauhan and R. Vaish, *Mater. Res. Express*, 2015, **1**, 045502.
17 B. Gong, F. Huang, Y. Shao, L. Lei, L. Liu, J. Wang, S. Yan, X. Lu and J. Zhu, *Phys. Status Solidi A*, 2020, **217**, 1900826.
18 Y. Tian, X. Chao, L. Wei, P. Liang and Z. Yang, *J. Appl. Phys.*, 2013, **113**, 184107.
19 Z. Wang, X. Chen, X. Chao, J. Wang, P. Liang and Z. Yang, *Ceram. Int.*, 2016, **42**, 18037–18044.
20 H. Palneedi, M. Peddigari, G. T. Hwang, D. Y. Jeong and J. Ryu, *Adv. Funct. Mater.*, 2018, **28**, 1803665.
21 S. Patel, D. Sharma, A. Singh and R. Vaish, *J. Materiomics*, 2016, **2**, 75–86.
22 T. M. Correia, M. McMillen, M. K. Rokosz, P. M. Weaver, J. M. Gregg, G. Viola and M. G. Cain, *J. Am. Ceram. Soc.*, 2013, **96**, 2699–2702.
23 M. Maraj, W. Wei, B. Peng and W. Sun, *Materials*, 2019, **12**, 3641.
24 D. Zhan, Q. Xu, D. P. Huang, H. X. Liu, W. Chen and F. Zhang, *J. Alloys Compd.*, 2016, **682**, 594–600.
25 V. S. Puli, D. K. Pradhan, D. B. Chrisey, M. Tomozawa, G. L. Sharma, J. F. Scott and R. S. Katiyar, *J. Mater. Sci.*, 2013, **48**, 2151–2157.
26 K. Xu, P. Yang, W. Peng and L. Li, *J. Alloys Compd.*, 2020, **829**, 154516.
27 Z. Hanani, S. Merselmiz, A. Danine, N. Stein, D. Mezzane, M. Amjoud, M. Lahcini, Y. Gagou, M. Spreitzer, D. Vengust, Z. Kutnjak, M. El Marssi, I. A. Luk'yanchuk and M. Gouné, *J. Adv. Ceram.*, 2020, **9**, 210–219.
28 M. Ben Abdessalem, I. Kriaa, A. Aydi and N. Abdelmoula, *Ceram. Int.*, 2018, **44**, 13595–13601.
29 J. Shi, R. Zhu, X. Liu, B. Fang, N. Yuan, J. Ding and H. Luo, *Materials*, 2017, **10**, 1093.
30 J. Wang, T. Yang, S. Chen, G. Li, Q. Zhang and X. Yao, *J. Alloys Compd.*, 2013, **550**, 561–563.
31 M. Sanlialp, V. V. Shvartsman, M. Acosta, B. Dkhil and D. C. Lupascu, *Appl. Phys. Lett.*, 2015, **106**, 5.
32 Y. Zhou, Q. Lin, W. Liu and D. Wang, *RSC Adv.*, 2016, **6**, 14084–14089.
33 Z. Kutnjak, B. Rožič and R. Pirc, in *Wiley Encyclopedia of Electrical and Electronics Engineering*, John Wiley & Sons, Inc., Hoboken, NJ, USA, 2015, pp. 1–19.
34 K. S. Srikanth, S. Patel and R. Vaish, *J. Aust. Ceram. Soc.*, 2018, **54**, 439–450.
35 Z. Hanani, D. Mezzane, M. Amjoud, Y. Gagou, K. Hoummada, C. Perrin, A. G. Razumnaya, Z. Kutnjak, A. Bouzina, M. El Marssi, M. Gouné and B. Rožič, *J. Mater. Sci.: Mater. Electron.*, 2020, **31**, 10096–10104.
36 Z. Hanani, E.-H. Ablouh, M. Amjoud, D. Mezzane, S. Fourcade and M. Gouné, *Ceram. Int.*, 2018, **44**, 10997–11000.
37 Z. Hanani, E. H. Ablouh, M. 'barek Amjoud, D. Mezzane, S. Fourcade and M. Gouné, *Ceram. Int.*, 2018, **44**, 10997–11000.
38 J. P. Praveen, T. Karthik, A. R. James, E. Chandrakala, S. Asthana and D. Das, *J. Eur. Ceram. Soc.*, 2015, **35**, 1785–1798.
39 P. Mishra, Sonia and P. Kumar, *J. Alloys Compd.*, 2012, **545**, 210–215.
40 A. Frattini, A. Di Loreto, O. de Sanctis and E. Benavidez, *Procedia Mater. Sci.*, 2012, **1**, 359–365.
41 Z. M. Wang, K. Zhao, X. L. Guo, W. Sun, H. L. Jiang, X. Q. Han, X. T. Tao, Z. X. Cheng, H. Y. Zhao, H. Kimura, G. L. Yuan, J. Yin and Z. G. Liu, *J. Mater. Chem. C*, 2013, **1**, 522–530.
42 P. Mishra, Sonia and P. Kumar, *Ceram. Int.*, 2014, **40**, 14149–14157.
43 B. Li, M. C. Ehmke, J. E. Blendell and K. J. Bowman, *J. Eur. Ceram. Soc.*, 2013, **33**, 3037–3044.
44 L. Zhang, M. Zhang, L. Wang, C. Zhou, Z. Zhang, Y. Yao, L. Zhang, D. Xue, X. Lou and X. Ren, *Appl. Phys. Lett.*, 2014, **105**, 162908.
45 C. H. Perry and D. B. Hall, *Phys. Rev. Lett.*, 1965, **15**, 700–702.
46 K. Jiang, P. Zhang, J. Zhang, G. Xu, W. Li, Z. Hu and J. Chu, *RSC Adv.*, 2016, **6**, 3159–3164.
47 B. D. Begg, K. S. Finnie and E. R. Vance, *J. Am. Ceram. Soc.*, 1996, **79**, 2666–2672.
48 W. Y. Zeng and A. Anderson, *J. Raman Spectrosc.*, 2001, **32**, 69–71.
49 X. Liu, M. Zhu, Z. Chen, B. Fang, J. Ding, X. Zhao, H. Xu and H. Luo, *J. Alloys Compd.*, 2014, **613**, 219–225.
50 N. Chaiyo, D. P. Cann and N. Vittayakorn, *J. Mater. Sci.*, 2015, **50**, 6171–6179.
51 W. Bai, D. Chen, P. Li, B. Shen, J. Zhai and Z. Ji, *Ceram. Int.*, 2016, **42**, 3429–3436.
52 X. W. Wang, B. H. Zhang, Y. C. Shi, Y. Y. Li, M. Manikandan, S. Y. Shang, J. Shang, Y. C. Hu and S. Q. Yin, *J. Appl. Phys.*, 2020, **127**, 074103.
53 Z. Wang, J. Wang, X. Chao, L. Wei, B. Yang, D. Wang and Z. Yang, *J. Mater. Sci.: Mater. Electron.*, 2016, **27**, 5047–5058.
54 W. Bai, D. Chen, J. Zhang, J. Zhong, M. Ding, B. Shen, J. Zhai and Z. Ji, *Ceram. Int.*, 2016, **42**, 3598–3608.
55 Y. Zhang, H. Sun and W. Chen, *J. Phys. Chem. Solids*, 2018, **114**, 207–219.
56 S. Hunpratub, S. Maensiri and P. Chindaprasirt, *Ceram. Int.*, 2014, **40**, 13025–13031.
57 V. S. Puli, D. K. Pradhan, I. Coondoo, N. Panwar, S. Adireddy, S. Luo, R. S. Katiyar and D. B. Chrisey, *J. Phys. D: Appl. Phys.*, 2019, **52**, 255304.
58 G. Ramesh, M. S. Ramachandra Rao, V. Sivasubramanian and V. Subramanian, *J. Alloys Compd.*, 2016, **663**, 444–448.
59 L. Eric Cross, *Ferroelectrics*, 1987, **76**, 241–267.
60 S. Tsukada, Y. Akishige, T. H. Kim and S. Kojima, *IOP Conf. Ser.: Mater. Sci. Eng.*, 2014, **54**, 012005.
61 Q. Xu, T. Li, H. Hao, S. Zhang, Z. Wang, M. Cao, Z. Yao and H. Liu, *J. Eur. Ceram. Soc.*, 2015, **35**, 545–553.
62 P. Butnoi, S. Manotham, P. Jaita, C. Randorn and G. Rujijanagul, *J. Eur. Ceram. Soc.*, 2018, **38**, 3822–3832.
63 A. R. Jayakrishnan, K. V. Alex, A. Thomas, J. P. B. Silva, K. Kamakshi, N. Dabra, K. C. Sekhar, J. Agostinho Moreira and M. J. M. Gomes, *Ceram. Int.*, 2019, **45**, 5808–5818.
64 W. Cai, Q. Zhang, C. Zhou, R. Gao, S. Zhang, Z. Li, R. Xu, G. Chen, X. Deng, Z. Wang and C. Fu, *J. Mater. Sci.: Mater. Electron.*, 2020, **31**(12), 9167–9175.

65 D. Zhan, Q. Xu, D. P. Huang, H. X. Liu, W. Chen and F. Zhang, *J. Phys. Chem. Solids*, 2018, **114**, 220–227.
66 S. Smail, M. Benyoussef, K. Taïbi, N. Bensemma, B. Manoun, M. El Marssi and A. Lahmar, *Mater. Chem. Phys.*, 2020, **252**, 123462.
67 S. Merselmiz, Z. Hanani, D. Mezzane, M. Spreitzer, A. Bradeško, D. Fabijan, D. Vengust, M. B. Amjoud, L. Hajji, Z. Abkhar, A. G. Razumnaya, B. Rožič, I. A. Luk'yanchuk and Z. Kutnjak, *Ceram. Int.*, 2020, **46**(15), 23867–23876.
68 Y. Lin, D. Li, M. Zhang, S. Zhan, Y. Yang, H. Yang and Q. Yuan, *ACS Appl. Mater. Interfaces*, 2019, **11**, 36824–36830.
69 T. Badapanda, S. Chaterjee, A. Mishra, R. Ranjan and S. Anwar, *Phys. B*, 2017, **521**, 264–269.
70 Z. Liu, X. Chen, W. Peng, C. Xu, X. Dong, F. Cao and G. Wang, *Appl. Phys. Lett.*, 2015, **106**, 262901.
71 R. A. Malik, A. Hussain, A. Maqbool, A. Zaman, T. K. Song, W. J. Kim and M. H. Kim, *J. Alloys Compd.*, 2016, **682**, 302–310.
72 B. Wang, L. Luo, X. Jiang, W. Li and H. Chen, *J. Alloys Compd.*, 2014, **585**, 14–18.
73 Z. Sun, Z. Wang, Y. Tian, G. Wang, W. Wang, M. Yang, X. Wang, F. Zhang and Y. Pu, *Adv. Electron. Mater.*, 2020, **6**, 1900698.
74 X. Wang, J. Wu, B. Dkhil, C. Zhao, T. Li, W. Li and X. Lou, *RSC Adv.*, 2017, **7**, 5813–5820.
75 X. Q. Liu, T. T. Chen, Y. J. Wu and X. M. Chen, *J. Am. Ceram. Soc.*, 2013, **96**, 1021–1023.
76 S. Patel, A. Chauhan and R. Vaish, *Phase Transitions*, 2016, **89**, 1019–1028.
77 R. Pirc, Z. Kutnjak, R. Blinc and Q. M. Zhang, *J. Appl. Phys.*, 2011, **110**, 074113.
78 B. Rožič, M. Kosec, H. Uršič, J. Holc, B. Malič, Q. M. Zhang, R. Blinc, R. Pirc and Z. Kutnjak, *J. Appl. Phys.*, 2011, **110**, 064118.
79 Y. Bai, X. Han and L. Qiao, *Appl. Phys. Lett.*, 2013, **102**, 1–5.
80 G. Singh, V. S. Tiwari and P. K. Gupta, *Appl. Phys. Lett.*, 2013, **103**, 202903.
81 S. Patel and R. Vaish, *Phase Transitions*, 2017, **90**, 465–474.
82 X. Zhang, L. Wu, S. Gao, J. Q. Liu, B. Xu, Y. D. Xia, J. Yin and Z. G. Liu, *AIP Adv.*, 2015, **5**, 047134.
83 G. Suchaneck, O. Pakhomov and G. Gerlach, in *Refrigeration*, InTech, 2017.
84 Y. Zhao, X. Q. Liu, S. Y. Wu and X. M. Chen, *J. Electroceram.*, 2019, **43**, 106–116.
85 W. P. Cao, W. L. Li, X. F. Dai, T. D. Zhang, J. Sheng, Y. F. Hou and W. D. Fei, *J. Eur. Ceram. Soc.*, 2016, **36**, 593–600.
86 X. S. Qian, H. J. Ye, Y. T. Zhang, H. Gu, X. Li, C. A. Randall and Q. M. Zhang, *Adv. Funct. Mater.*, 2014, **24**, 1300–1305.
87 S. G. Lu and Q. Zhang, *Adv. Mater.*, 2009, **21**, 1983–1987.
88 A. Kumar, A. Thakre, D. Y. Jeong and J. Ryu, *J. Mater. Chem. C*, 2019, **7**, 6836–6859.
89 R. Kumar and S. Singh, *J. Alloys Compd.*, 2018, **764**, 289–294.
90 Y. Zhao, X. Hao and Q. Zhang, *Ceram. Int.*, 2016, **42**, 1679–1687.
91 R. Kumar, A. Kumar and S. Singh, *Sustainable Energy Fuels*, 2018, **2**, 2698–2704.
92 R. Kumar and S. Singh, *Sci. Rep.*, 2018, **8**, 3186.
93 R. Kumar, D. Khurana, A. kumar and S. Singh, *Ceram. Int.*, 2018, **44**, 20845–20850.
94 B. Peng, Q. Zhang, B. Gang, G. J. T. Leighton, C. Shaw, S. J. Milne, B. Zou, W. Sun, H. Huang and Z. Wang, *Energy Environ. Sci.*, 2019, **12**, 1708–1717.
95 E. Defay, S. Crossley, S. Kar-Narayan, X. Moya and N. D. Mathur, *Adv. Mater.*, 2013, **25**, 3337–3342.
96 Y. Zhao, X. Hao and Q. Zhang, *ACS Appl. Mater. Interfaces*, 2014, **6**, 11633–11639.
97 X. Hao, Y. Zhao and Q. Zhang, *J. Phys. Chem. C*, 2015, **119**, 18877–18885.
98 H. Gao, X. Hao, Q. Zhang, S. An and L. B. Kong, *J. Mater. Sci.: Mater. Electron.*, 2016, **27**, 10309–10319.